Hydrol. Earth Syst. Sci. Discuss., 12, 12567–12613, 2015
www.hydrol-earth-syst-sci-discuss.net/12/12567/2015/
doi:10.5194/hessd-12-12567-2015

Hydrology and Earth System Sciences
Open Access
Discussions

Sequential hydraulic tests for transient and highly permeable unconfined aquifer systems – model development and field-scale implementation

C.-F. Ni[1], Y.-J. Huang[1], J.-J. Dong[1], and T.-C. J. Yeh[2]

[1]Graduate Institute of Applied Geology, National Central University, Taoyuan City, Taiwan
[2]Department of Hydrology and Water Resources, The University of Arizona, Tucson, USA

Received: 21 October 2015 – Accepted: 9 November 2015 – Published: 4 December 2015

Correspondence to: C.-F. Ni (nichuenfa@geo.ncu.edu.tw, nichuenf@gmail.com)

Published by Copernicus Publications on behalf of the European Geosciences Union.

Abstract

The transient hydraulic tomography survey (THTS) is a conceptually improved technique that efficiently estimates detailed variations in aquifer parameters. Based on the concept of the THTS, we developed a geostatistical inverse model to characterize saturated hydraulic conductivity (K) and the specific yield (Sy) in transient and unconfined aquifer systems. In this study, a synthetic example was first used to assess the accuracy of the developed inverse model. Multiple random K and Sy realizations with different variances of natural logarithm of K ($\ln K$) were generated and systematically compared to evaluate the effects of joint inversion on K estimations. The model was implemented in field-scale, cross-hole injection tests in a shallow and highly permeable unconfined aquifer near the middle reaches of the Wu River in central Taiwan. To assess the effect of constant head boundary conditions on the estimation results, two additional modeling domains were evaluated on the basis of the same field data from the injection tests. The results of the synthetic example showed that the proposed inverse model can effectively reproduce the predefined K patterns and magnitudes. However, slightly less detail was obtained for the Sy field based on the sampling data from sequential transient hydraulic stresses. The joint inversion by using transient head observations could slightly decrease the accuracy of K estimations. The model implementation for field-scale injection tests showed that the model can estimate K and Sy fields with detailed spatial variations. Estimation results showed a relatively homogeneous aquifer for the tested well field. Results based on the three modeling domains showed similar patterns and magnitudes of K and Sy near the well locations. These results indicated that the THTS is relatively insensitive to artificially drawn boundary conditions even under transient conditions.

HESSD
12, 12567–12613, 2015

1 Introduction

Conventional approaches to obtain the hydraulic conductivity values (K) and the storage coefficients (S) for aquifers rely on slug or pumping tests and the associated well developed analytical or semi-analytical solutions. These approaches can be used to efficiently estimate either averaged aquifer parameters (i.e., pumping or injection tests) between wells or point measurements (slug tests) near wells. Because of the sizes of representative control volumes driven by local stresses, these approaches are insensitive to aquifer strata connectivity (Bohling et al., 2007; Bohling and Butler, 2010). Previous studies have recognized that the great challenge to characterize groundwater flow and transport remains the limited measurements. The small numbers of measurements for most practical problems, therefore, have motivated the development of sequential cross-hole tests and associated inverse models to maximize the usefulness of measurements (Zhu and Yeh, 2005; Bohling et al., 2007; Illman et al., 2008; Cardiff et al., 2009; Ni and Yeh, 2008; Ni et al., 2009).

Tomographic approaches such as hydraulic and pneumatic tomography surveys have been proven to be feasible techniques for estimating aquifer properties with detailed spatial variations on different scales (Bohling et al., 2007; Cardiff and Barrash, 2011; Berg and Illman, 2011, 2014). In the past two decades numerous models have been developed for application to hydraulic tests for the laboratory or field-scale experiments (Gottlieb and Dietrich, 1995; Yeh and Liu, 2000; Zhu and Yeh, 2005; Cardiff et al., 2009, 2012; Schöniger et al., 2012; Mao et al., 2013). With the improvement of measuring and computing technologies, previous studies have focused on the development of efficient inverse models to solve problems with realistic scales and complexities. Gottlieb and Dietrich (1995) used a least squares optimization algorithm to estimate the spatial distribution of hydraulic conductivity in a synthetic two-dimensional saturated aquifer. In their study, the steady-state condition was considered by assigning the storage coefficient as zero. A similar tomography concept coupled with a stochastic approach for inversion was used in the study of Kitanidis (1995). Yeh

HESSD
12, 12567–12613, 2015

and Liu (2000) developed a sequential stochastic inverse model called the sequential successive linear estimator (SSLE). Their model can be applied to hydraulic tests for aquifers under confined and steady-state conditions. The optimization algorithm in the SSLE relies on the simulation of sensitivity equations for flow, and the algorithm iteratively updates cokriging weightings to obtain a conditional K field. The advantage of the sequential inclusion of pumping tests is the computational efficiency because the sequential pumping or injection events are calculated separately and are integrated by inner iteration loops. The sizes of the matrices for sensitivity simulations are considerably reduced. Subsequently, Zhu and Yeh (2005) improved the SSLE to solve transient flow problems. The SSLE inverse model was tested successfully for laboratory experiments (Liu et al., 2002, 2007; Illman et al., 2008, 2010, 2012) and field studies (Bohling et al., 2007; Straface et al., 2007; Illman et al., 2009; Berg and Illman, 2011, 2014).

Detailed distributions of K and Sy in unconfined aquifers are critical for predicting near-surface contaminant transport and for quantifying surface water–ground water interactions. Estimating aquifer properties for unconfined aquifers is difficult because of the complexity of drawdown behavior to be fitted and the nonlinearity of the flow equation to be solved (Mao et al., 2011). The study of Cardiff et al. (2009) focused on a potential-based approach and used the Dupuit–Forchheimer assumption to analyze pumping test data from fully screened wells in an unconfined aquifer at the Boise Hydrogeophysical Research Site (BHRS). The quasilinear Bayesian geostatistical inverse method developed by Kitanidis (1995) was used to optimize the distribution of depth-averaged hydraulic conductivity. The advantage of the potential-based approach is that the unconfined nonlinear flow equation can be transformed to a linear one and can be solved using a typical optimization algorithm. Subsequently, the study of Cardiff and Barrash (2011) summarized the investigations of the hydraulic tomography survey for two- and three-dimensional problems and used numerical experiments to assess the effect of the storage coefficient and the geostatistical parameters on estimating K values in transient unconfined aquifer systems. Their numerical experiments showed

HESSD
12, 12567–12613, 2015

that the estimation of K was slightly degraded if joint estimations of storage parameters were required. The numerical model was also implemented in a field-scale inverse problem at the BHRS (Cardiff et al., 2012).

With the development of measurement technologies and associated analyzing algorithms, it can be expected that high-quality and -quantity data can be obtained in laboratories or on-site. The sequential hydraulic test is a practical, feasible technique for aquifer characterization. The model used for such aquifer tests should meet operation procedures and high-resolution requirements (Ni and Yeh, 2008; Ni et al., 2009). The objectives of our study were threefold: (1) to develop a cross-hole inverse model for characterizing groundwater flow in transient and unconfined aquifers, (2) to develop a well field and conduct a field-scale experiment following the characterization procedures proposed in the inverse model, and (3) to implement the developed inverse model to characterize the hydraulic tests from the well field. More specifically, in this study, we modified the SSLE program developed by Zhu and Yeh (2005) and Ni and Yeh (2008) to estimate two-dimensional depth-averaged distributions of K and Sy for transient and unconfined aquifer systems. In this study, we first derived the SSLE model for transient flow in an unconfined aquifer system. Our model is similar to the concept of Ni and Yeh (2008); however, different mathematical formulas were used to account for the responses of transient and unconfined aquifer systems. This study developed an iterative procedure to solve the nonlinear mean flow equations and the associated nonlinear adjoint state equations. We then tested the developed inverse model by using a synthetic example. Multiple random K and Sy realizations were then used to evaluate the accuracy of the model for reduced conditioning points and joint estimations of K and Sy. The developed model was implemented to field-scale hydraulic tests to estimate the K and Sy distributions for the well field.

HESSD
12, 12567–12613, 2015

2 Flow equations

Consider groundwater flow in a transient, depth-averaged, two-dimensional, and heterogeneous unconfined aquifer system. The governing equation for the flow in such an unconfined aquifer system can be represented by

$$\mathrm{Sy}\frac{\partial h}{\partial t} = \nabla\cdot(T\nabla h) + q_\mathrm{s} \tag{1}$$

subject to the initial condition

$$h(\boldsymbol{x},0) = h_0(\boldsymbol{x}) \qquad \boldsymbol{x}\in\Omega \tag{2}$$

and the boundary conditions

$$h(\boldsymbol{x},t) = h_\mathrm{f}(\boldsymbol{x},t) \qquad \boldsymbol{x}\in\Gamma_D \tag{3}$$

$$(K\nabla h)\cdot\overline{\boldsymbol{n}}(\boldsymbol{x}) = q_\mathrm{b}(\boldsymbol{x},t) \qquad \boldsymbol{x}\in\Gamma_N \tag{4}$$

where $h = h(\boldsymbol{x},t)$ is the hydraulic head [ℓ], $\boldsymbol{x}$ is the vector of Cartesian coordinates $(x,y)^T$, and t is the time. The aquifer parameter $T(\boldsymbol{x}) = K(\boldsymbol{x})h(\boldsymbol{x})$ is the transmissivity [ℓ^2/t], where $K(\boldsymbol{x})$ is hydraulic conductivity [ℓ/t], which is assumed to be homogeneous throughout the depth of the aquifer. The symbol $\mathrm{Sy} = \mathrm{Sy}(\boldsymbol{x})$ is the specific yield. The notation $q_\mathrm{s} = q_\mathrm{s}(\boldsymbol{x},t)$ refers to the depth-averaged source or the sink term for the aquifer system. In Eqs. (3) and (4), $h_\mathrm{f}(\boldsymbol{x},t)$ is the specified head on the boundary segment Γ_D, $q_\mathrm{b} = q_\mathrm{b}(\boldsymbol{x},t)$ is the flux across the Neumann boundary Γ_N, and $\overline{\boldsymbol{n}}$ is an outward unit vector normal to Γ_N. Because the transmissivity involves unknown head values, Eq. (1) is a nonlinear equation for transient two-dimensional unconfined aquifer systems. To solve this equation, the Galerkin finite element method and Conjugate gradient matrix solver were used to solve Eq. (1). An iteration algorithm involving inner iterative loops at each time step is employed to obtain the solution of h for the nonlinear equation. This nonlinearity can also lead to nonlinearity of a series of equations for the inversion procedure.

HESSD
12, 12567–12613, 2015

3 Optimization algorithm

Numerous approaches have been developed in previous studies to solve inverse problems based on the data from field-scale pumping or slug tests. These approaches follow the general concept of using the observed hydraulic head $h(\boldsymbol{x}, t)$ to estimate the value of hydraulic conductivity $K(\boldsymbol{x})$ based on the minimization of an objective function for differences between observed and simulated heads (Mclaughlin and Townley, 1996; Vargas-Guzmân and Yeh, 1999). The SSLE uses the similar concept; however, a series of hydraulic tests is integrated on the basis of the knowledge of geostatistical regularization. The SSLE starts with the classical cokriging operation to calculate the nonlinear relationship between head and hydraulic conductivity but focuses on minimizing the residual head and sequentially incorporates the pumping or injection data from different stresses. Iterations are used to ensure that the estimations best fit the observations from different stresses that rely on the sensitivity equations. A detailed description of the sequential processes can be found in the studies of Yeh and Liu (2000), Ni and Yeh (2008), and Mao et al. (2013).

To estimate flow properties such as K and Sy in a transient and unconfined aquifer system, we assume that the spatial distributions of the natural logarithm of K and Sy (i.e., $\ln K$ and $\ln \mathrm{Sy}$) in unconfined aquifers are stochastic processes. The K and Sy values are composed of mean values and the associated small perturbations. Mathematical formulas are represented as $\ln K = \overline{f} + f'$ and $\ln \mathrm{Sy} = \overline{g} + g'$, where $\overline{f}$ and $\overline{g}$ are the mean values, and f' and g' are the perturbations. The transient head responses to an injection or pumping test are also treated as stochastic processes and can be represented by $h = \overline{h} + h'$, where $\overline{h}$ is the mean head and h' is the perturbation. Following the procedures proposed by Yeh and Liu (2000), we assume that the source or sink term q_s (i.e., the pumping or injection in the aquifer) in this study is considered to be a deterministic process. Substituting the stochastic variables into Eq. (1) and taking the expectation yields the following mean equation for a transient and unconfined

HESSD
12, 12567–12613, 2015

aquifer:

$$\mathrm{Sy}_\mathrm{c}\frac{\partial \overline{h}_\mathrm{c}}{\partial t} = \nabla\cdot\left[\overline{K}_\mathrm{c}\overline{h}_\mathrm{c}\nabla\overline{h}_\mathrm{c}\right] + \nabla\cdot\left[\overline{K}_\mathrm{c}\langle h'_\mathrm{c}\nabla h'_\mathrm{c}\rangle\right] + \overline{K}_\mathrm{c}\overline{h}_\mathrm{c}\langle\nabla f'_\mathrm{c}\nabla h'_\mathrm{c}\rangle + \overline{K}_\mathrm{c}\nabla\overline{h}_\mathrm{c}\langle h'_\mathrm{c}\nabla f'_\mathrm{c}\rangle + \overline{\mathrm{Sy}}_\mathrm{c}\left\langle f'_\mathrm{c}\frac{\partial h'_\mathrm{c}}{\partial t} - g'_\mathrm{c}\frac{\partial h'_\mathrm{c}}{\partial t}\right\rangle + q_\mathrm{s} \quad (5)$$

where subscript c denotes the condition of variables, angle brackets represent the expectation of variables, and $\overline{K}_\mathrm{c}$, $\overline{h}_\mathrm{c}$, and $\overline{\mathrm{Sy}}_\mathrm{c}$ are conditional hydraulic conductivity, hydraulic head, and specific yield, respectively. Additional terms on the right hand side of Eq. (5) represent the contribution of perturbations f' and h' to the estimation of the conditional mean flow. Similar to the approach of Yeh and Liu (2000), we assume that the second to the fourth terms on the right hand side of Eq. (5) are proportional to the mean head gradient. Moreover, the fifth term on the right hand side of Eq. (5) is proportional to temporal variations in the mean head. The approximation procedure has been commonly used in previous studies to formulate a simple version of the stochastic mean flow (Gelhar, 1993; Rubin, 2003) and implement to complex flow problems (Ni and Li, 2009; Ni et al., 2011ab). Such manipulations lead to the following conditional mean equation for groundwater flow in a transient and unconfined aquifer system:

$$\overline{\mathrm{Sy}}_\mathrm{eff}\frac{\partial \overline{h}_\mathrm{c}}{\partial t} = \nabla\cdot\left[\overline{K}_\mathrm{eff}\overline{h}_\mathrm{c}\nabla\overline{h}_\mathrm{c}\right] + q_\mathrm{s} \quad (6)$$

where $\overline{K}_\mathrm{eff}$ and $\overline{\mathrm{Sy}}_\mathrm{eff}$ are the conditional effective hydraulic conductivity and the conditional effective specific yield, respectively. This mean equation has the same form as Eq. (1); however, it is expressed with the conditional effective conductivity, conditional mean hydraulic head, and conditional effective specific yield. The term $\overline{K}_\mathrm{eff}$ in Eq. (5) is a parameter that integrates the effect of the conditional mean conductivity $\overline{K}_\mathrm{c}$ and the ratio of the second to fourth terms to the conditional mean head gradient.

HESSD
12, 12567–12613, 2015

The parameter $\overline{Sy}_{eff}$ combines the conditional specific yield $\overline{Sy}_c$ and the effect of the f', g', and h' on temporal variations in the conditional mean head.

To obtain the $\overline{K}_{eff}$ and $\overline{Sy}_{eff}$ in Eq. (6), the kriged K and Sy fields based on available K and Sy measurements and the initial guess of the geostatistical structure are used for calculating the head distributions. The cokriging algorithm is then used to integrate the available head measurements from different stresses sequentially. During the iteration through stresses and the associated observations, the model updates the geostatistical structure by modifying the covariance matrices. Parameters for a transient unconfined aquifer system are estimated using the following steps:

1. Select a stress event and the associated head observations. Apply initial guesses of K and Sy values to the simulation domain. Typical values are the kriged K and Sy based on direct measurements of K and Sy at sites. The forward simulation then provides simulated hydraulic heads for the simulation domain on the first attempt.

2. Collect the simulated heads at locations where the observations (i.e., the hydraulic heads) are available. Calculate the head differences between the simulated and observed heads. These head differences are called residual heads in this study. Incorporate the head differences and the observed K and Sy in a cokriging interpolation to updated $\ln K$ and $\ln \mathrm{Sy}$ fields. In this step, the geostatistical structure and the associated parameters for the cokriging estimation are the initial guess values.

3. Run a forward simulation on the basis of the updated $\ln K$ and $\ln \mathrm{Sy}$ fields. The differences between simulated and observed heads are then recalculated. This process can be considered as the first iteration for the first stress event. We consider this flow field as the conditional mean flow (i.e., the solution of Eq. 6), and the mean flow is used for sensitivity estimations in the next step.

HESSD
12, 12567–12613, 2015

4. Use the adjoint state method to solve sensitivity equations. The sensitivity matrices are then used to calculate the cokriging covariance matrices for residual heads and the cross-covariances for residual head, $\ln K$, and $\ln Sy$.

5. Update the $\ln K$ and $\ln Sy$ fields by using the cokriging interpolation and the associated covariance and cross-covariance matrices from the previous step.

6. Check convergence of the estimation for current stress and the associated head observations. This study uses the summation of residual heads and the cokriging error variance as the convergence criteria for each stress. If the summation of the residual heads or the change in cokriging variance meets the predefined convergence criteria, a different stress event and the associated head observations are selected. The estimation process then repeats steps 3–6 until all the stresses are involved in the estimation. Typically, the change in cokriging error variances is rigidly bound to stop the iterations for each stress event.

4 Sensitivity estimations for covariance matrices

Calculation of the covariance of heads and the cross-covariance of heads and $\ln K$ and $\ln Sy$ requires the determination of the sensitivity matrices. This study used the adjoint state method to conduct sensitivity analyses (Sykes et al., 1985; Sun, 1994). The detailed derivation of the adjoint state approach can be found in the study of Sykes et al. (1985) for steady-state confined aquifer systems, in the study of Zhu and Yeh (2005) for transient confined aquifer systems, and in the study of Ni and Yeh (2008) for gas phase flows in unsaturated porous media. In this study, we derived the adjoint state equation for a transient unconfined aquifer system. The adjoint state sensitivities are based on the governing Eqs. (1)–(4). Following similar derivations to those proposed by Ni and Yeh (2008), the adjoint state equation for a transient and unconfined aquifer

HESSD
12, 12567–12613, 2015

is given by the following formula:

$$\mathrm{Sy}\frac{\partial \psi}{\partial t} + \nabla \cdot [K h \nabla \psi] - K \nabla h \nabla \psi + \delta(x - x_k)(t - t_l) = 0 \quad (7)$$

subject to the boundary and initial conditions:

$$\psi|_{\Gamma_D} = 0, \quad (8)$$

$$[K \nabla \psi] \cdot \overline{\boldsymbol{n}}|_{\Gamma_N} = 0, \quad (9)$$

and

$$\psi|_{t=0} = 0 \quad (10)$$

In Eqs. (7)–(10), ψ is an arbitrary function used for estimating the state sensitivity for the observation at location x_k or at time t_l, where subscripts k and l represent the indices of locations and times for head observations, respectively. Notations $\delta(x - x_k)$ and $\delta(t - t_l)$ are the delta functions. The solutions for Eqs. (7)–(10) can be obtained by solving the conditional mean head equation (i.e., Eq. 6). The third term in Eq. (7) reflects the nonlinearity of the unconfined flow equation. The number of simulations for Eq. (7) depends on the number of spatial and temporal head observations. Under this condition, the sensitivity of the head at location x_k and time t_l to $\ln K$ at location x_n are given by

$$\frac{\partial h(x_k, t_l)}{\partial \ln K(x_n)} = \iint_{\Omega\Gamma} \left\{ \frac{\partial K}{\partial \ln K}[h \nabla h \nabla \psi] + \frac{\partial \mathrm{Sy}}{\partial \ln K}\left[\psi \frac{\partial h}{\partial t}\right] \right\} \mathrm{d}t\mathrm{d}\Omega \quad (11)$$

In this study, dependent parameters K and Sy are considered to be uncorrelated and the Sy in Eq. (11) is not a function of K; Eq. (11) can be reduced to the following formula:

$$\frac{\partial h(x_k, t_l)}{\partial \ln K(x_n)} = \iint_{\Omega\Gamma} \frac{\partial K}{\partial \ln K}[h \nabla h \nabla \psi] \mathrm{d}t\mathrm{d}\Omega \quad (12)$$

HESSD
12, 12567–12613, 2015

Eqation (11) is slightly different from the equations derived by Yeh and Liu (2000) and Zhu and Yeh (2005) for confined steady and confined transient aquifers. Again, an additional appearance of the variable h shown in the bracket of Eq. (12) reflects the nonlinearity of the unconfined flow equation. A similar procedure can be applied to obtain the sensitivity of the head at location x_k and time t_l to $\ln \mathrm{Sy}$ at location x_n, which is given by

$$\frac{\partial h(x_k, t_l)}{\partial \ln \mathrm{Sy}(x_n)} = \iint_{\Omega\Gamma} \left\{ \frac{\partial K}{\partial \ln \mathrm{Sy}} [h \nabla h \nabla \psi] + \frac{\partial \mathrm{Sy}}{\partial \ln \mathrm{Sy}} \psi \frac{\partial h}{\partial t} \right\} \mathrm{d}t \mathrm{d}\Omega \tag{13}$$

Under the condition that K and Sy are uncorrelated and K in Eq. (13) is not a function of Sy, the sensitivity of the head at location x_k and time t_l to $\ln \mathrm{Sy}$ at location x_n gives the following:

$$\frac{\partial h(x_k, t_l)}{\partial \ln \mathrm{Sy}(x_n)} = \iint_{\Omega\Gamma} \left[\frac{\partial Sy}{\partial \ln \mathrm{Sy}} \psi \frac{\partial h}{\partial t} \right] \mathrm{d}t \mathrm{d}\Omega \tag{14}$$

The cross-covariance matrices can be obtained by incorporating the sensitivities (i.e., Eqs. 12 and 14) with covariances of $\ln K$ and $\ln \mathrm{Sy}$. Detailed derivations of the covariances and the cokriging equations using the sensitivity in Eqs. (12) and (14) can be found in the studies of Yeh and Liu (2000) and Mao et al. (2013). For each pumping or injection test, the conditional parameters $\overline{K}_{\mathrm{eff}}$ and $\overline{\mathrm{Sy}}_{\mathrm{eff}}$ are successively estimated on the basis of evaluations of the sensitivities and the statistical structure. Similar to the numerical method used in the flow equations, Galerkin finite element method and Conjugate gradient matrix solver were used to solve adjoint state equations for sensitivities. In the following sections, the estimated aquifer parameters were denoted as $\ln K$ and $\ln \mathrm{Sy}$ for presentation purpose.

HESSD
12, 12567–12613, 2015

5 Numerical examples

To verify the developed model for estimating K (or T) and Sy in transient unconfined aquifers, we first tested the developed model by using a numerical base example. The scale of modeling domain and values of aquifer mean K and Sy for the base example are similar to those of our well field. The estimations of the unconfined aquifer parameters $\ln K$ and $\ln \mathrm{Sy}$ were based on the generated synthetic head observations. To assess the effects of conditioning points and joint inversion of K and Sy on the estimation results, additional testing cases were created by using the simulation domain same as that in base example but with varied conditioning points and random K and Sy realizations. The following sections present the conceptual model and the associated numerical and geostatistical conditions for the numerical base example and testing cases.

5.1 Model description

5.1.1 Numerical base example

In the numerical base example, the aquifer has a size of 40 m × 20 m and a constant thickness of 10 m. Figure 1 shows the generated synthetic $\ln K$ and $\ln \mathrm{Sy}$ fields. In this study, the $\ln K$ and $\ln \mathrm{Sy}$ fields were generated using the Fast Fourier Transform algorithm (Deutsch and Journel, 1997) on the basis of an exponential covariance model. The variances of $\ln K$ and $\ln \mathrm{Sy}$ for the exponential covariance model in random field generation were 1.0 and 0.1, respectively. Isotropic correlation lengths for the $\ln K$ and $\ln \mathrm{Sy}$ fields were fixed at 10 m in the exponential covariance model. Under the predefined conditions for random field generation, the generated K values ranged from 5 to 200 $\mathrm{m\,d^{-1}}$. However, the values of Sy varied from 0.05 to 0.16.

Figure 1a also shows the conceptual model of the numerical example. The constant head conditions were specified along the northern and southern boundaries. Five pumping wells and 10 monitoring wells were installed in the simulation area (Fig. 1b).

HESSD
12, 12567–12613, 2015

The uniform finite element mesh for this example was 1 m × 1 m. Such element size required 800 elements and 861 nodes to cover the entire simulation area. To generate the synthetic head observations to test our model, this study conducted forward simulations on the basis of a constant pumping rate applied to the locations of the pumping wells (as marked by circles in Fig. 1b). A steady-state model was conducted to obtain the initial condition for the transient forward simulation. The time step for the simulation was fixed to 0.002 d and the total simulation time for each stress was 0.04 d. For each pumping event, the transient head observations were then collected from the observation wells (as marked by triangles in Fig. 1b). The contour lines shown in Fig. 1a represent one of the pumping events applied to the pumping well in the upper right corner of the simulation domain. In this study the random measurement errors were not considered in the synthetic head observations. The technical difficulty to include all the transient head observations in the inverse model has led to comprehensive studies of sampling strategies to reproduce effectively the original head observations (Ni and Yeh, 2009; Cardiff and Barrash, 2011; Sun et al., 2013). Following the general concept in previous studies, we then selected two head observations in the early, middle, and, late time intervals for joint inversion of the predefined $\ln K$ and $\ln Sy$ fields shown in Fig. 1. These sampling times are 0.002, 0.004, 0.008, 0.01, 0.036, and 0.04 d, respectively. Such sampling times and numerical parameters are used for the following testing cases.

5.1.2 Testing cases for reduced conditioning points

Following same procedures to generate head observations for $\ln K$ and $\ln Sy$, the tested cases for varied conditioning points use the random $\ln K$ and $\ln Sy$ fields same as those in the base example. However, the numbers of conditioning points for $\ln K$ and $\ln Sy$ were varied from the original 15 points (in the base example) to one point. Using the $\ln K$ and $\ln Sy$ fields same as those in the base example, the selected numbers of conditioning points for the testing cases are 11, 8, 5, 3, and 1, respectively. For each specified number of conditioning points, we used five random sets of $\ln K$ and $\ln Sy$

HESSD
12, 12567–12613, 2015

conditioning points to evaluate the averaged performance of the estimations. In this study the available locations to specify the conditioning points were fixed to the 15 well locations shown in the base example.

5.1.3 Testing cases for accuracy of ln$K$ estimations using joint inversion of transient head observations

The developed inverse model are flexible to allow ln$K$ and ln Sy fields to be estimated jointly using transient simulations or allow ln$K$ fields to be estimated using steady-state simulations. A checking process for transient data was developed in the inverse model to avoid misuse of simulation types. To assess the accuracy of ln$K$ estimations using transient and steady-state head observations, the transient head observations generated in each testing case were considered for joint estimations of ln$K$ and ln Sy fields (denoted as Case 1) and also considered for estimation of ln$K$ fields (denoted as Case 2). However, the last transient head data at observation wells during each stress in Case 1 were used in Case 2 for steady-state estimation of a ln$K$ field. We are particularly interested in the effect of different ln$K$ variability on the joint inversion results. Four ln$K$ variances, including 0.5, 1.0, 1.5, and 2.0, were considered in the testing cases. However, the testing cases have a fixed ln Sy variance of 0.1 and mean Sy of 0.1.

For a specified ln$K$ variance, we generated 10 random ln$K$ and ln Sy fields and conducted forward simulations to obtain the synthetic transient head observations. Similar to the forward simulation in the base example, the initial conditions for different random ln$K$ and ln Sy fields need to be simulated with a steady-state model. The selected head observations for the inversion follow the strategy used in the base example. The joint inversions of the ln$K$ and ln Sy fields (i.e., the Case 1) rely on the generated transient head observations. For estimating solely the ln$K$ fields (i.e., the Case 2), the steady-state inversions were conducted and the last temporal head observations of different pumping stresses in Case 1 were considered. The selections of the head observations in Case 1 might directly influence the ln$K$ estimations in

HESSD
12, 12567–12613, 2015

Case 2. In this study, the influences had been implicitly considered in the comparisons of $\ln K$ estimations in Cases 1 and 2.

5.2 Results and discussion of numerical examples

5.2.1 Numerical base example

Figure 2 presents the results estimated using the developed inverse model. With a total of 25 iterations (five iterations for each pumping stress), the developed inverse model could capture the patterns and magnitudes of the generated $\ln K$ and $\ln Sy$ fields (Fig. 1). To quantitatively evaluate the accuracy of the inverse model, the scatterplots in Fig. 3 show the element-by-element values for $\ln K$ and $\ln Sy$ from the synthetically generated fields and the model-estimated fields. L1 and L2 in Fig. 3 represent the mean absolute error normal and mean square error normal, respectively. The correlation coefficient of the generated and estimated parameters is based on the following formula:

$$\text{Correl}(\theta, \theta^*) = \frac{1}{n-1} \frac{\sum_{i=1}^{n} \left(\theta_i - \overline{\theta}\right)\left(\theta_i^* - \overline{\theta^*}\right)}{\sigma_{\theta_i} \sigma_{\theta_i^*}} \tag{15}$$

where $\overline{\theta}$ and $\overline{\theta^*}$ represent the means of parameters. Notations σ_{θ_i} and $\sigma_{\theta_i^*}$ are standard deviations for the two parameters ($\ln K$ and $\ln Sy$). Based on the definition of the correlation value, this value represents the overall normalized difference between the simulated and generated $\ln K$ or $\ln Sy$ field. The L1 and L2 values reflect the overall relative errors between the estimated and the generated $\ln K$ or $\ln Sy$ field. The variance of $\ln K$ for generating the $\ln K$ field was 1.0, and the variance for generating the $\ln Sy$ field was only 0.1. Simulation results implies that the inverse model and the associated sampling strategy might lead to a better estimation of $\ln K$ because of the relatively high variability of generated $\ln K$ field as compared with the generated $\ln Sy$ field.

HESSD
12, 12567–12613, 2015

Figure 4 shows the comparisons of observed and simulated head perturbations at well locations for five pumping events. The observed data were the head observations generated on the basis of the synthetic $\ln K$ and $\ln S_y$ fields. Most observation heads were within the range of 7.8–8.0 m because the boundary conditions in the base example were fixed in this range. The values below 7.8 m (less than −0.2 head perturbations) showed the observation data near or at the pumping wells. Figure 5 shows the distributions of cokriging error variances for $\ln K$ and $\ln S_y$ from our model. In the synthetic example, we assigned known $\ln K$ and $\ln S_y$ values at the locations of monitoring and pumping wells. These $\ln K$ and $\ln S_y$ values were considered to be the conditioning points and were incorporated in the cokriging iterations. The results clearly reflect relatively low error variance values at these locations. The error variance values for $\ln S_y$ were generally lower than those for $\ln K$, because we used a relatively low variance value to generate the $\ln S_y$ field. We found that the specified head conditions along the north and south boundaries could lead to relatively low values of cokriging error variance for $\ln K$. One explanation for such low error variance values along specified head boundaries is the fixed head values at the boundaries. The fixed head values along the boundaries are deterministically assigned and the variance of heads should be small. The contribution of the $\ln K$ error variance values is mainly from the head gradient along the constant head boundaries (see Eq. 12). In $\ln S_y$ estimations, the relatively low cokriging error variances were only obtained near the conditioning points (i.e., at the pumping and monitoring wells). The contribution of the sensitivity of head to $\ln S_y$ depends on temporal variations of heads (see Eq. 14).

5.2.2 Testing cases for reduced conditioning points

The results for the random selections of conditioning points were summarized in Fig. 6. Each specified number of conditioning points is the averaged value based on five random selections of condition points in the simulation domain. We assume that the selected well locations have the observed $\ln K$ and $\ln S_y$ values. The results in Fig. 6 clearly show decreasing trends of the estimation errors and increasing trends

HESSD
12, 12567–12613, 2015

of correlation for $\ln K$ and $\ln Sy$. This is common knowledge in the inverse modeling that the numbers of conditioning points significantly control the results of parameter estimations. However, the distributions of the $\ln K$ and $\ln Sy$ fields could be crucial for the estimation results.

In the testing cases, we found significant changes of estimation errors and correlation for 8 and 5 conditioning points. Such results are particularly obvious in estimations of $\ln K$. The results of $\ln Sy$ show relatively gradual changes of the estimation errors and correlation values. In this study the observed results are based on the complexity of $\ln K$ and $\ln Sy$ fields in the base example (Fig. 1). For field-scale experiments that have similar scale and geostatistical parameters, the 8 conditioning points could be the key information for consideration of experiment and model efficiency. In practical applications, the conditioning point (i.e., the K or Sy value at a well location) requires a direct measurement of K or Sy with a relatively small-scale. However, the effects of well conditions and accuracy of measurement techniques might directly influence the results of K or Sy at the well field.

5.2.3 Testing cases for accuracy of $\ln K$ estimations using transient and steady-state head observations

Figure 7 presents the comparisons of estimated $\ln K$ for different estimation strategies. In Fig. 7a and b, we found relatively low estimation errors for $\ln K$ estimations by using the steady state model (i.e., Case 2). The differences of the estimation errors increase with the increasing $\ln K$ variances. The correlations show identically the values and decreasing trend from low to high values of $\ln K$ variances (Fig. 7c). Except for the $\ln K$ variance value of 1.5, the estimation strategy in Case 2 shows consistently higher correlations of $\ln K$ than those in Case 1. However, the correlations for the variance value of 1.5 in Cases 1 and 2 are 0.8071 and 0.8023, respectively. This slightly difference might be influenced by the generated random $\ln K$ and $\ln Sy$ fields and the sampled data that we used for joint inversion of $\ln K$ and $\ln Sy$. The comparison of $\ln K$ estimations in Cases 1 and 2 is useful to judge the role of additional transient

HESSD
12, 12567–12613, 2015

head data for joint inversion. In this study we assumed that the distributions of the ln$K$ and ln Sy fields are uncorrelated to derived Eqs. (12) and (14) for sensitivity matrices. These sensitivity matrices are the fundamental elements of cross-covariance function for sequential cokriging estimations. Theoretically, the estimations of ln$K$ and ln Sy must be solely depending on the head observations for joint inversion (i.e., Case 1). Our simulation results indicate that the redundant head observations might slightly reduce the accuracy of ln$K$ estimations.

Figure 7c further shows the correlations for estimated ln Sy in Case 1. The values of ln Sy correlation increase with the increasing ln$K$ variances. The increasing tend is obvious as compared with the decreasing correlations of ln$K$ for different ln$K$ variances. Note that the variance of generated ln Sy fields was fixed to 0.1 in this study. The mechanism of how the ln Sy correlations decrease with the decreasing ln$K$ variances is not clear and might require additional case studies to clarify the relationship between ln$K$ and ln Sy in the joint inversion.

6 Field-scale implementation

The previous section showed that the developed model could be used to estimate synthetic ln$K$ and ln Sy fields with accurate patterns and magnitudes. In most situations, the pumping tests can be replaced by injection tests, depending on the conditions at the site of interest. In this study, we developed a well field in a highly permeable unconfined aquifer for field-scale implementation of the developed model. The scale and the boundary conditions for the experiments were similar to those in the synthetic examples. However, because of limited thickness of the saturated zone at the test site and limited well diameters for the installation of high-capacity pumps, cross-hole injection tests were conducted to obtain head observations.

HESSD
12, 12567–12613, 2015

6.1 Site description

The rivers in Taiwan are mainly in the east–west direction because of high mountain areas in the central portion of the island. The crucial characteristics of river flows in Taiwan are the short concentration times and steep slopes. Such behaviors generally lead to large grain sizes of river deposits, and river discharges are highly variable between wet and dry seasons. The study area was in the middle reaches of the Wu River in Central Taiwan. Figure 8 shows the location of our well field by the south side of the Wu River. The unconfined aquifer materials at the test site are mainly alluvial deposits from the Holocene period. The aquifer in this area is mainly composed of gravel, sand, and silt, with thicknesses varying from 7 to 10 m near the test site. Based on site investigations and analyses of soil samples from well logs, these gravel deposits can be categorized as well-graded gravel with sand and silt (GW-GM) according to the Unified Soil Classification System (USCS) originally developed by Casagrande (1948). The Pliocene Cholan Formation was identified as being present below the unconfined aquifer. The Cholan Formation in this area is composed of interbedded sandstone and shale. Dong et al. (2010) conducted permeability tests for rock samples in the Cholan Formation in this area. Results showed that the hydraulic conductivity of the Cholan Formation varied from 10^{-2} to 10^{-5} m d^{-1}. A four-orders-of-magnitude difference was observed in hydraulic conductivity values between the river deposits and the bedrock in the Cholan Formation. Because of the relatively low hydraulic conductivity of the Cholan Formation, the interface between the Cholan Formation and the alluvium deposits was considered to be a no-flow bottom boundary in our numerical model.

The average groundwater table at the test site was 2.4 m below the ground surface. In this study, a total of 15 wells, including 5 injection wells and 10 monitoring wells, were installed in the well field for our field-scale injection tests. Figure 9 shows the distributions of developed wells at the experimental site. The wells in our well field all had the same depth of 10 m, and the well screens were opened through the unconfined

HESSD
12, 12567–12613, 2015

aquifer. In addition, 4 inch and 2 inch PVC tubes were installed for the injection and monitoring wells, respectively. In Fig. 9, well names starting with "DP" represent the injection wells, and the names starting with "DW" indicate the monitoring wells. The numbers below the well names are the depths below the ground surface at which the interface between the Cholan Formation and the alluvial deposits was identified.

6.2 Cross-hole injection test

The tested aquifer was highly permeable, and the pumping test at the research site required a high-capacity pump (approximately 400 $L\,min^{-1}$) to produce sufficient drawdowns for observations. Because of the limited well size (4 in) to install the high-capacity pump, we then conducted cross-hole injection tests in this study. The injected water was obtained from an irrigation channel near the well field. To determine the injection rate for our injection tests, we conducted a pretest for each injection well before the sequential injection tests. Based on the well conditions and the conductivity of the material near injection wells, the injection rate selected should be able to induce sufficient head increments (several centimeters) in most observation wells. A constant flow rate of 400 $L\,min^{-1}$ was then selected for all of the injection wells.

Figure 10 shows the time series of selected head observations from our injection tests. We used pressure sensors to monitor the head values in both monitoring and injection wells for the injection tests. With sequential switching of the injection wells, 14 head variation time series were observed for each injection event. Figure 10a, c, and e shows the head increments at injection wells (i.e., the DP wells), and Fig. 10b, d, and f shows selected head time series of monitoring wells (i.e., the DW wells). During the injection test, we found that the head changes at the injection wells increased dramatically at the beginning (less than 60 s) of the injection. Only the DP9801 well showed a gradual increase in head increments at the injection well (Fig. 10a). However, the monitoring wells always showed gradually increasing head increments. During the injection tests, the head observations at injection wells were monitored in real time, and the injections were stopped when relatively small changes were observed in heads at

HESSD
12, 12567–12613, 2015

injection wells. In the case of injection at the DP9801 well, the power generator was unexpectedly shut off after 500 s during the injection experiment. The observations for this situation were also included in the parameter estimation processes. The head observations from the injection wells were not included in our simulations because we did not have sufficient information to judge if the highly fluctuating head variations at injection wells can be used for parameter inversions. Such head observations might be influenced by well bore effects or other factors during the installation of the wells.

6.3 Parameter estimations

In this study, the boundary and initial conditions of the simulation area were defined on the basis of the interpolation and extrapolation of water level measurements in the well field. The values of constant head boundaries at the experiment site were slightly lower than those for our synthetic examples. The initial mean K value for the parameter estimations was based on the averaged K values from two falling head slug tests conducted at the DP9802 and DP9804 wells. In the model, we assumed that K and Sy data (or conditioning points) were not available at injection and monitoring wells. However, the model required at least a boundary value (i.e., a conditioning point) for the inverse model to be solvable. An artificial conditioning point was then assigned at the left down corner of the simulation area to make less influence of the conditioning point on parameter estimations. The conditioning K and Sy values at the locations were $50.2\,\mathrm{m\,d^{-1}}$ and 0.1, respectively. These values are the same as the initial mean K and Sy for the model. The K and Sy values at the point were fixed through the calculation processes. Table 1 summarizes the input and initial values of the modeling parameters for the field-scale experiment. Note that the input geostatistical structures are the initial guesses for sequential cokriging interpolations in the inverse model. With the updated covariance matrices estimated by adjoint state method, the geostatistical structure are modified to honor the head observations.

The sampling time interval for head observations in this study was fixed at 1 s. Based on the quantity of data obtained from our cross-hole experiments, it was

HESSD
12, 12567–12613, 2015

computationally difficult to include all the head time series in the inverse model because of the storage and calculation of covariance matrices. We followed the suggestions of Ni and Yeh (2009) and Cardiff and Barrash (2011), that key observations in early, middle, and the late time intervals are sufficient to effectively reproduce the aquifer parameters. For observations from each monitoring well, we then selected two head observations in the early time interval (less than 60 s), two head observations in the middle time interval (between 60 and 200 s), and two observations in the late time interval (between 500 and 1000 s). Different selections of head observations may lead to slightly different parameter estimations. However, the patterns of the parameter distributions should be similar. A detailed comparison of different sampling strategies can be found in the study of Sun et al. (2013).

Figure 11 shows the distributions of the estimated $\ln K$ and $\ln Sy$ fields for the test site. The K values varied from 10 to 100 ($m\,d^{-1}$), and the Sy values ranged from 0.02 to 0.16. The patterns of the $\ln K$ field were complex, and high $\ln K$ zones were located along the north boundary and near the well locations. By comparing the estimated K values with the slug tests conducted at the DP9802 and DP9804 wells, the range of the estimated K values appeared to be accurate. Additionally, the initial geostatisctical structure for $\ln K$ field was assumed to be isotropic (see Table 1). We found that the high $\ln K$ zones showed anisotropy patterns with slightly greater correlation in the x direction. Such results indicated that the geostatistical structure near the well field had been modified based on the head observations. The pattern of the $\ln Sy$ distribution was relatively simple. A high $\ln Sy$ zone was found near the DP9804 and DW9806 wells. We hypothesize that these high $\ln K$ or $\ln Sy$ zones may be relevant to the development of the well field. This situation is faced in most investigations. In this study, we did not focus on the validation of well installation processes at this site. Our objective was to test whether the developed model could be applied to field-scale problems.

Figure 12 shows the results for the cokriging error variance after 25 iterations (five iterations for each injection event) for $\ln K$ (Fig. 12a) and $\ln Sy$ (Fig. 12b). Because no conditioning point was assigned at the well locations, the results reflect only the

HESSD
12, 12567–12613, 2015

estimation error variances based on the head observations. The results in Fig. 12a show high cokriging error variance areas in the central portion of the model domain. Although the low $\ln K$ areas showed slightly larger error variances, the differences in the cokriging error variances were extremely close (Figs. 11a and 12a). These results are similar to the $\ln Sy$ estimations shown in Figs. 11b and 12b. We also found relatively low $\ln K$ error variances along the two constant head boundary conditions. The constant head boundary condition might be a crucial factor influencing the $\ln K$ error variances. To evaluate the effect of the constant head boundaries on the estimation results, two additional models with expanded domain sizes were conducted, and their results are compared in detail in the next section.

6.4 Boundary effect on parameter estimations

Two additional models were developed for evaluating the effect of the constant head boundaries on the estimation results. Figure 13 shows the sizes and boundary conditions for the three models. Among the two additional models, the largest 70 m × 50 m model was named Model 1, and the 50 m × 30 m model was named Model 2. The original model with the size of 40 m × 20 m was named Model 3. Because head observations were not available for assigning the constant head boundary conditions, we then used boundary head values that were extrapolated on the basis of head observations from the well field. This approximation procedure is the same as that used for the original model. Detailed information of all the boundary conditions is shown in Fig. 13. We used the same grid space of the computational mesh for the two large models. Based on the mesh size of 1 m × 1 m, the number of elements was 3500 for Model 1 and 1500 for Model 2. The original model (Model 3) had an element number of 800. The origins of the two additional models were all switched to (0, 0) for comparison purposes.

Figures 14 and 15 show the results based on the same head observations at well locations. We are particularly interested in the area of the well field (i.e., the area surrounding the wells) because the head observations in these areas were available

HESSD
12, 12567–12613, 2015

for $\ln K$ and $\ln Sy$ estimations. In Fig. 14, all three models with different sizes clearly showed low $\ln K$ zones in the central portions of the well fields. High $\ln K$ values were observed in the north portion of the well field. Despite the different sites of the modeling domain, the patterns of estimated $\ln K$ fields near the well field remain similar, and the determinations of $\ln K$ values away from the well fields were computed with the iterated and updated cokriging covariance matrices. This result is consistent with that of Sun et al. (2013), indicating that the tomography concept can map regions beyond the immediate vicinity of the wells. The unexpected high and low $\ln K$ values outside the well field might be caused by the numerical accuracy of the inversion process. A similar conclusion can be applied to the $\ln Sy$ results shown in Fig. 15. Similar patterns were observed for the $\ln Sy$ fields in the three models. High $\ln Sy$ zones were observed in the northwest portions of the well fields. We further extracted the estimated $\ln K$ and $\ln Sy$ values in Models 1 and 2 and compared the estimated $\ln K$ and $\ln Sy$ values with those of Model 3. The element-by-element comparisons were limited to the same area in Model 3. In general, the correlations between Models 3 and 2 and between Models 3 and 1 are higher than 0.95. Figure 16 shows the comparisons of observed vs. simulated transient head values at selected well locations. The values of mean absolute error norm (L1) and mean square error normal (L2) were extremely close in the three models. Based on the results of the comparisons, we suggest that Model 3 with the smallest modeling domain of 40 m × 20 m is sufficient for the test site. In this simulation domain, the distance of boundary conditions is 5 m away from the well locations.

In this study, it is worth mentioning the computational issue for the developed model and the expanded simulation domains. In general, approximately 80 % of the computational time was used for estimating sensitivity matrices by using the adjoint state method. Because the head changes were not significant, only two to three iterations were generally required to obtain convergent solutions for the nonlinear mean head and adjoint state equations (i.e., Eqs. 6 and 7). Based on our workstation with Intel Xeon 2.0 GHz CPU and 12 MB memory, the computational times for the three models were in the order of min for Model 3, in the order of hour for Models 2 and 1.

HESSD
12, 12567–12613, 2015

This result clearly shows that the sizes of simulation domains dramatically increased the computational effort required to solve the mean head and adjoint state equations. However, in this study, the improvement of estimated $\ln K$ and $\ln Sy$ fields near the wells was not significant.

7 Conclusions

In this study, we developed a two-dimensional inverse model for transient and unconfined aquifers on the basis of the concept of sequential cokriging interpolation. Here, the governing equations for sensitivity estimations of flow in transient and unconfined aquifer systems were reformulated, and the associated programs were developed to solve the nonlinear conditional mean flow and adjoint state equations. The numerical examples and testing cases in this study showed that the developed model could detect detailed spatial variations in $\ln K$ and $\ln Sy$ based on the generated aquifer parameters and the associated head observations. With the selected head observations in the early, middle, and late time intervals from monitoring wells, the sequential inclusions of head measurements from different pumping events can reproduce the predefined $\ln K$ and $\ln Sy$ fields with acceptable accuracy.

The distributions of cokriging error variances for the numerical example showed significantly different mechanisms for $\ln K$ and $\ln Sy$ estimations. Except for the predefined conditioning points in the numerical example, relatively low values were obtained for the $\ln K$ cokriging error variances along the constant head boundaries. Unlike the results of the $\ln K$ cokriging error variances, the $\ln Sy$ cokriging error variances were not influenced by the constant head boundaries.

The accuracy of the estimated $\ln K$ and $\ln Sy$ fields reduced with the reduced conditioning points applied to the inverse model. For the predefined $\ln K$ and $\ln Sy$ fields, significant changes of estimation errors and correlation were observed for a number of conditioning points. This significant drops of the number of conditioning points could be the key information for consideration of experiment and modeling

HESSD
12, 12567–12613, 2015

efficiency. The comparisons of estimated $\ln K$ for different estimation strategies showed relatively low estimation errors for steady state model. The differences of the estimation errors can increase with the increasing $\ln K$ variances. Such results indicated that the redundant transient head observations might slightly reduce the accuracy of $\ln K$ estimations.

In this study, we developed a well field for field-scale injection tests. The depth-averaged field injection tests were then conducted for the model implementation. Simulation results show that the pattern of the estimated $\ln K$ distribution for the test site is complex. The pattern of $\ln Sy$ distribution is relatively simple. However, all the $\ln K$ and $\ln Sy$ values varied by only one order of magnitude, indicating that the test site is a relatively homogeneous aquifer. The comparison of expanded simulation domains for injection tests showed that three models with different domain sizes clearly present similar patterns of $\ln K$ and $\ln Sy$ distributions near the well locations. On the basis of the model tests for three domain sizes, we found that the THTS is relatively insensitive to artificially drawn boundary conditions even under transient conditions.

Acknowledgements. This research was partially supported by the National Science Council of the Republic of China under grants NSC 100-2625-M-008-005-MY3 and NSC 100-2116-M-008-005 and the Water Resources Agency, Ministry of Economic Affairs under grant MOEAWRA0980060.

References

Berg, S. J. and Illman, W. A.: Three-dimensional transient hydraulic tomography in a highly heterogeneous glaciofluvial aquifer-aquitard system, Water Resour. Res., 47, W10507, doi:10.1029/2011WR010616, 2011.

Berg, S. J. and Illman, W. A.: Comparison of hydraulic tomography with traditional methods at a highly heterogeneous site, Ground Water, 53, 71–89, doi:10.1111/gwat.12159, 2014.

Bohling, G. and Butler, J.: Inherent limitations of hydraulic tomography, Ground Water, 48, 809–824., 2010.

HESSD
12, 12567–12613, 2015

Bohling, G. C., Butler, J. J., Zhan, X. Y., and Knoll, M. D.: A field assessment of the value of steady shape hydraulic tomography for characterization of aquifer heterogeneities, Water Resour. Res., 43, W05430, doi:10.1029/2006WR004932, 2007.
Cardiff, M. and Barrash, W.: 3-D transient hydraulic tomography in unconfined aquifers with fast drainage response, Water Resour. Res., 47, W12518, doi:10.1029/2010WR010367, 2011.
Cardiff, M., Barrash, W., Kitanidis, P., Malama, B., Revil, A., Straface, S., and Rizzo, E.: A potential-based inversion of unconfined steady-state hydraulic tomography, Ground Water, 47, 259–270, 2009.
Cardiff, M., Barrash, W., and Kitanidis, P.: A field proof-of-concept of aquifer imaging using 3-D transient hydraulic tomography with temporarily-emplaced equipment, Water Resour. Res., 48, W05531, doi:10.1029/2011WR011704, 2012.
Casagrande, A.: Classification and identification of soils, T. Am. Soc. Civ. Eng., 113, 901–930, 1948.
Deutsch, C. V. and Journel, A. G.: GSLIB Geostatistical Software Library and User's Guide, Oxford University Press, New York, 1997.
Dong, J. J., Hsu, J. Y., Wu, W. J., Shimamoto, T., Hung, J. H., Yeh, E. C., Wu, Y. H., and Sone, H.: Stress-dependence of the permeability and porosity of sandstone and shale from TCDP Hole-A, Int. J. Rock Mech. Min., 47, 1141–1157, 2010.
Gelhar, L. W.: Stochastic Subsurface Hydrology, Prentice-Hall, Englewood Cliffs, NJ, 1993.
Gottlieb, J. and Dietrich, P.: Identification of the permeability distribution in soil by hydraulic tomography, Inverse Probl., 11, 353–360, 1995.
Illman, W. A., Craig, A. J., and Liu, X.: Practical issues in imaging hydraulic conductivity through hydraulic tomography, Ground Water, 46, 120–132, 2008.
Illman, W. A., Zhu, J. F., Craig, A. J., and Yin, D. T.: Comparison of aquifer characterization approaches through steady state groundwater model validation: a controlled laboratory sandbox study, Water Resour. Res., 46, W04502, doi:10.1029/2009WR007745, 2010.
Illman, W. A., Berg, S. J., and Yeh, T. C. J.: Comparison of approaches for predicting solute transport: sandbox experiments, Ground Water, 50, 421–431, 2012.
Kitanidis, P. K.: Quasi-linear geostatistical theory for inversing, Water Resour. Res., 31, 2411–2419, 1995.
Liu, S. Y., Yeh, T. C. J., and Gardiner, R.: Effectiveness of hydraulic tomography: sandbox experiments, Water Resour. Res., 38, 5-1–5-9 , doi:10.1029/2001WR000338, 2002.

HESSD
12, 12567–12613, 2015

Liu, X., Illman, W. A., Craig, A. J., Zhu, J., and Yeh, T. C. J.: Laboratory sandbox validation of transient hydraulic tomography, Water Resour. Res., 43, W05404, doi:10.1029/2006WR005144, 2007.

Mao, D., Wan, L., Yeh, T. C. J., Lee, C. H., Hsu, K. C., Wen, J. C., and Lu, W.: A revisit of drawdown behavior during pumping in unconfined aquifers, Water Resour. Res., 47, W05502, doi:10.1029/2010WR009326, 2011.

Mao, D., Yeh, T.-C. J., Wan, L., Wen, J.-C., Lu, W., Lee, C.-H., and Hsu, K.-C.: Joint interpretation of sequential pumping tests in unconfined aquifers, Water Resour. Res., 49, 1782–1796, doi:10.1002/wrcr.20129, 2013.

McLaughlin, D. and Townley, L. R.: A reassessment of the groundwater inverse problem, Water Resour. Res., 32, 1131–1161, 1996.

Ni, C. F. and Li, S. G.: Approximate analytical solution to groundwater velocity variance in unconfined trending aquifers in the presence of complex sources and sinks, J. Hydrol. Eng., 14, 1119–1125, 2009.

Ni, C. F. and Yeh, T. C. J.: Stochastic inversion of pneumatic cross-hole tests and barometric pressure fluctuations in heterogeneous unsaturated formations, Adv. Water Resour., 31, 1708–1718, 2008.

Ni, C. F., Yeh, T. C. J., and Chen, J. S.: Cost-effective hydraulic tomography surveys for predicting flow and transport in heterogeneous aquifers, Environ. Sci. Technol., 43, 3720–3727, 2009.

Ni, C.-F., Lin, C.-P., Li, S.-G., and Chen, J.-S.: Quantifying flow and remediation zone uncertainties for partially opened wells in heterogeneous aquifers, Hydrol. Earth Syst. Sci., 15, 2291–2301, doi:10.5194/hess-15-2291-2011, 2011a.

Ni, C. F., Lin, C. P., Li, S. G., and Liu, C. J.: Efficient approximate spectral method to delineate stochastic well capture zones in nonstationary groundwater flow systems, J. Hydrol. 407, 184–195, 2011b.

Rubin, Y.: Applied Stochastic Hydrogeology, Oxford University Press, New York, 2003.

Schöniger, A., Nowak, W., and Franssen, H. J. H.: Parameter estimation by ensemble Kalman filters with transformed data: approach and application to hydraulic tomography, Water Resour. Res., 48, W04502, doi:10.1029/2011WR010462, 2012.

Straface, S., Yeh, T., Zhu, J., Troisi, S., and Lee, C.: Sequential aquifer tests at a well field, Montalto Uffugo Scalo, Italy, Water Resour. Res., 43, W07432, doi:10.1029/2006WR005287, 2007.

HESSD
12, 12567–12613, 2015

Sun, N.-Z.: Inverse Problems in Groundwater Modeling: Theory and Applications of Transport Porous Media, Kluwer Academic, Dordrecht, Boston, 1994.

Sun, R., Yeh, T.-C. J., Mao, D., Jin, M., Lu, W., and Hao, Y.: A temporal sampling strategy for hydraulic tomography analysis, Water Resour. Res., 49, 3881–3896, doi:10.1002/wrcr.20337, 2013.

Sykes, J. F., Wilson, J. L., and Andrews, R. W.: Sensitivity analysis for steady-state groundwater-flow using adjoint operators, Water Resour. Res., 21, 359–371, 1985.

Vargas-Guzman, J. A. and Yeh, T. C. J.: Sequential kriging and cokriging: two powerful geostatistical approaches, Stoch. Env. Res. Risk A., 13, 416–435, 1999.

Yeh, T. C. J. and Liu, S.: Hydraulic tomography: development of a new aquifer test method, Water Resour. Res., 36, 2095–2105, 2000.

Zhu, J. F. and Yeh, T. C. J.: Characterization of aquifer heterogeneity using transient hydraulic tomography, Water Resour. Res., 41, W07028, doi:10.1029/2004WR003790, 2005.

HESSD
12, 12567–12613, 2015

Table 1. Input and initial values of the parameter estimations for the field-scale experiment.

Parameter	ln$K$ estimation	ln Sy estimation
covariance model	exponential	exponential
mean value	50.2 m d^{-1}	0.01
variance	0.5	0.1
x correlation length	20 m	20 m
y correlation length	20 m	20 m

HESSD
12, 12567–12613, 2015

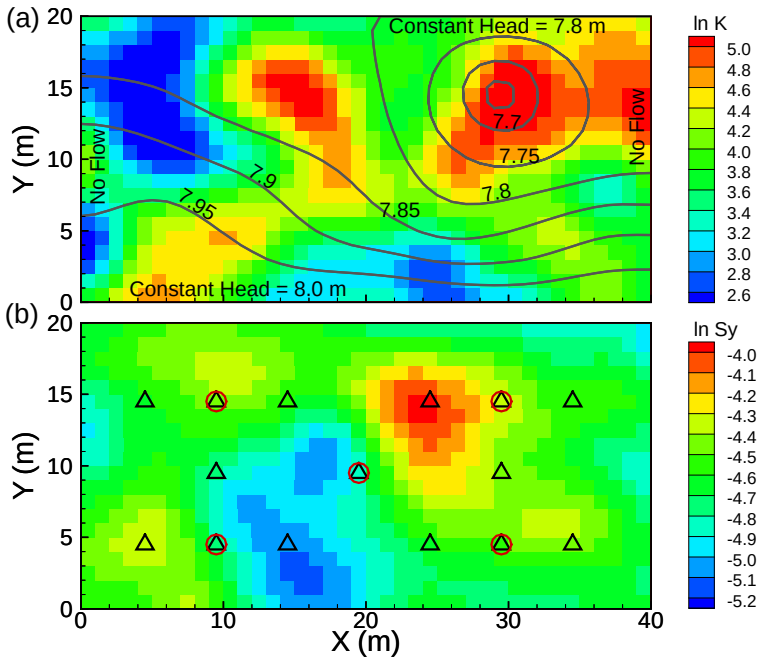

Figure 1. The generated **(a)** ln$K$ and **(b)** ln Sy fields for the numerical base example. The head contours in **(a)** show one of the pumping tests applied to the well at (30, 15). Constant head boundary conditions were specified along the north and south boundaries, and a flow boundary condition was assigned along the east and west boundaries. The symbols in **(b)** indicate the pumping (circle) and observation (triangle) wells.

HESSD
12, 12567–12613, 2015

Sequential hydraulic tests for transient unconfined aquifers

C.-F. Ni et al.

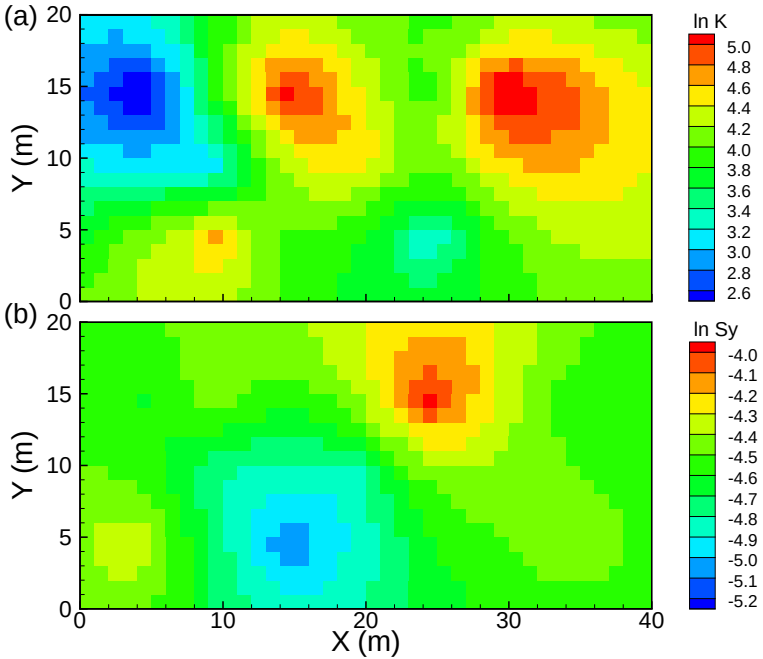

Figure 2. The estimated **(a)** ln$K$ and **(b)** ln Sy fields for the numerical base example.

HESSD
12, 12567–12613, 2015

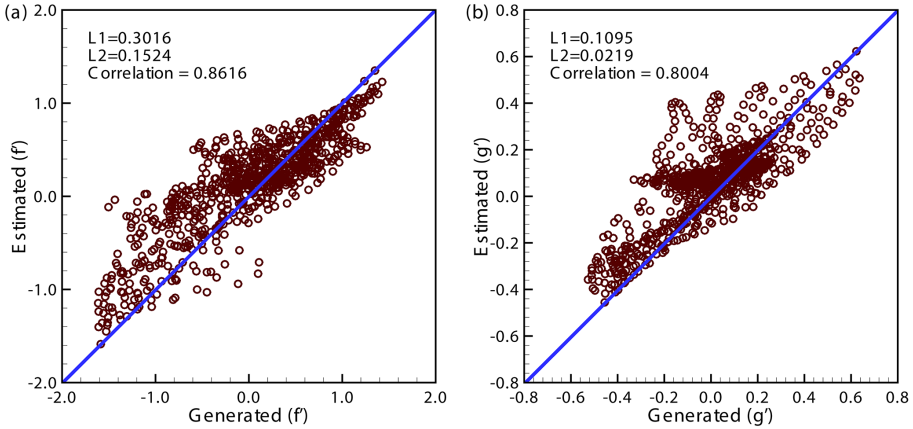

Figure 3. Scatter plots for a direct comparison of generated and estimated parameter perturbations about the means: **(a)** generated vs. estimated $\ln K$ perturbations and the associated error analysis. **(b)** Generated vs. estimated $\ln Sy$ perturbations and the associated error analysis. L1 and L2 represent the mean absolute error norm and the mean square error norm, respectively.

HESSD
12, 12567–12613, 2015

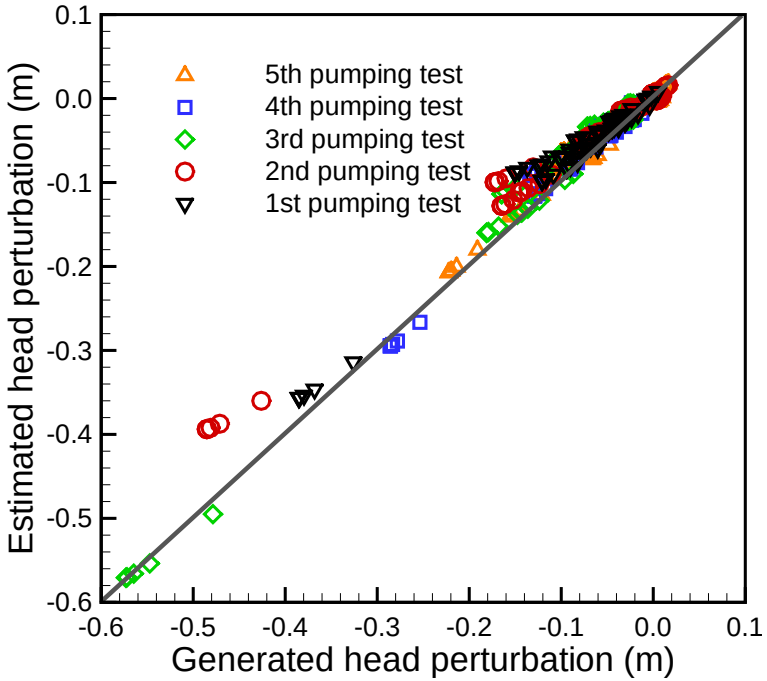

Figure 4. Comparison of observed and simulated head variations for five pumping events.

HESSD
12, 12567–12613, 2015

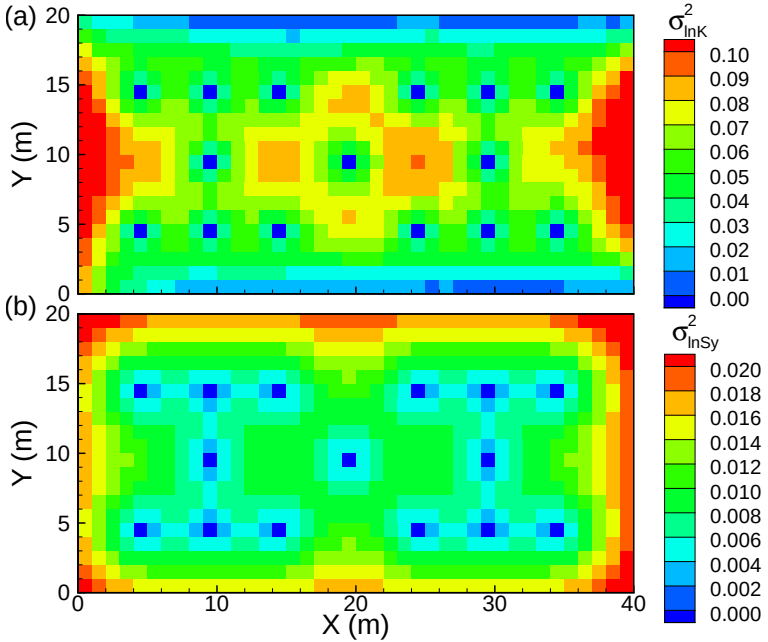

Figure 5. Distributions of error variances for **(a)** ln K and **(b)** ln Sy after inversion in the numerical base example.

HESSD
12, 12567–12613, 2015

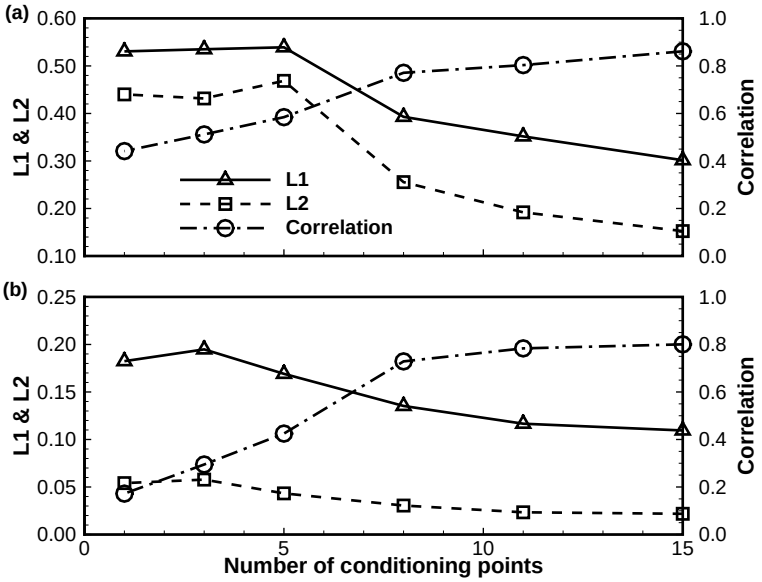

Figure 6. The L1, L2, and correlation for testing cases with reduced conditioning points: **(a)** ln*K* and **(b)** ln Sy.

HESSD
12, 12567–12613, 2015

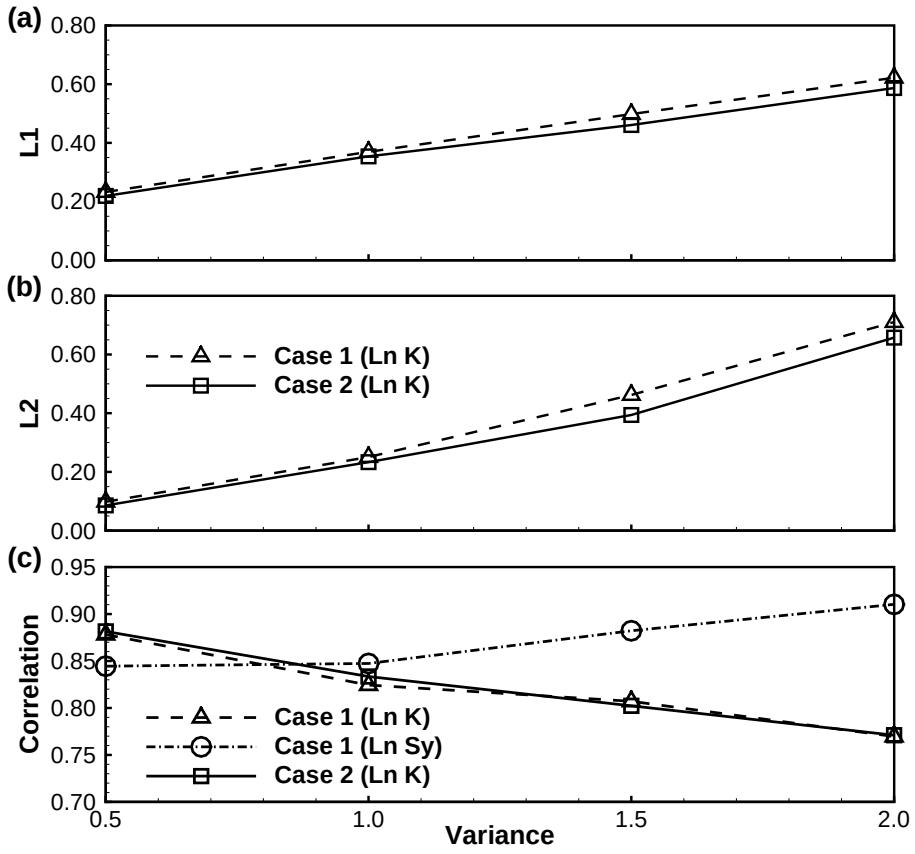

Figure 7. Comparisons of estimated $\ln K$ for joint inversion based on transient model (Case 1) and individual inversion based on steady state model (Case 2): **(a)** L1, **(b)** L2, and **(c)** element-by-element correlation between generated and the estimated $\ln K$ values.

HESSD
12, 12567–12613, 2015

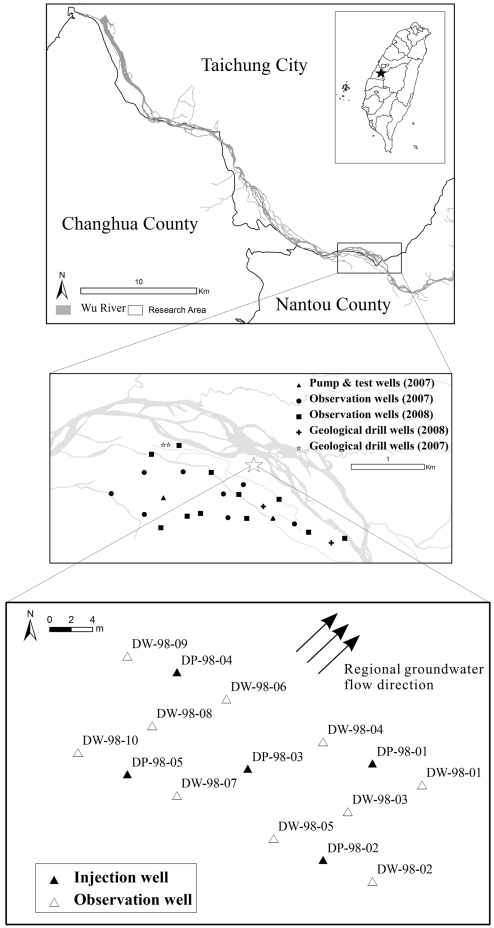

Figure 8. Location of the well field for the field-scale injection tests in this study. The wells were developed in a 20 m × 40 m area by the south side of the Wu River in central Taiwan.

HESSD
12, 12567–12613, 2015

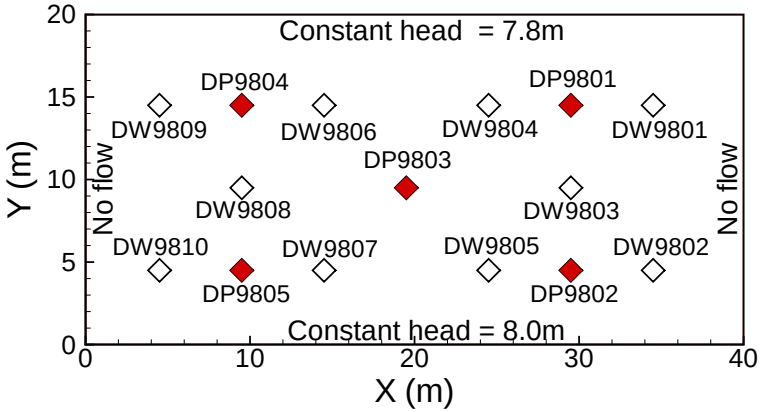

Figure 9. Distribution of installed wells at the experimental site. In this study, a total of 15 wells were installed in the well field for our field-scale injection tests. The numbers below the well names indicate the depths (in meters) where the interfaces between the Cholan Formation and the alluvium deposits were identified. ND stands for "not detected". This condition shows that the interface at the well location can be greater than the well length 10 m.

HESSD
12, 12567–12613, 2015

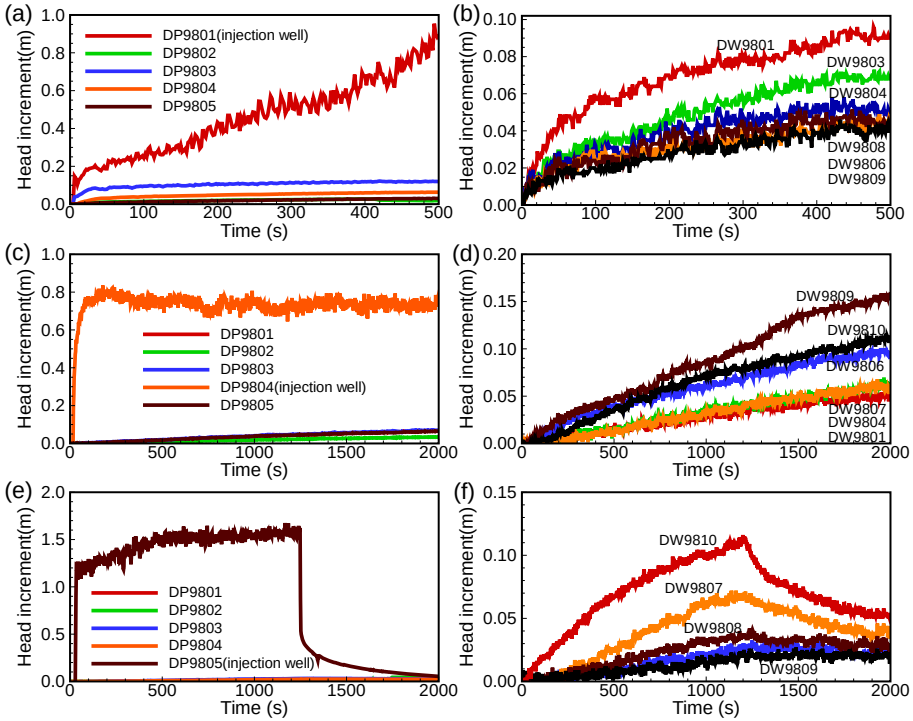

Figure 10. Time series of selected head observations from three injection tests conducted at the research well field.

HESSD
12, 12567–12613, 2015

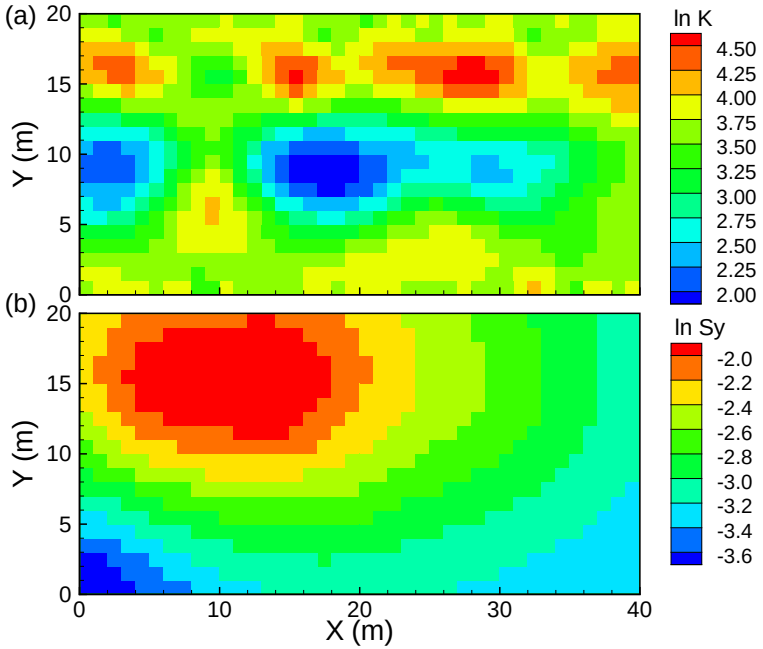

Figure 11. Distributions of the estimated **(a)** ln$K$ and **(b)** ln Sy for the test site. The hydraulic conductivity varied from 10 to 100 ($m\,d^{-1}$), and the specific yield values were in the range of 0.02 and 0.16.

HESSD
12, 12567–12613, 2015

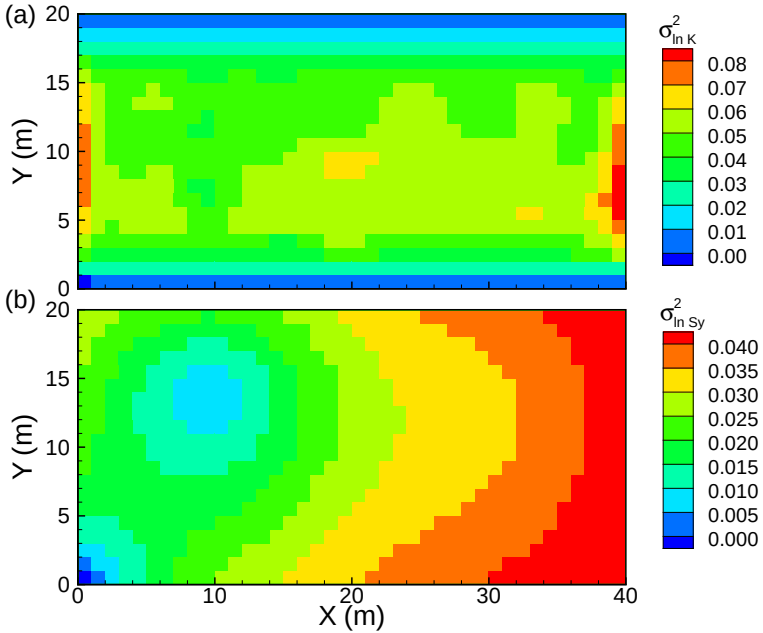

Figure 12. Distributions of cokriging error variances for **(a)** ln$K$ and **(b)** ln Sy after 25 iterations (five iterations for each injection event).

HESSD
12, 12567–12613, 2015

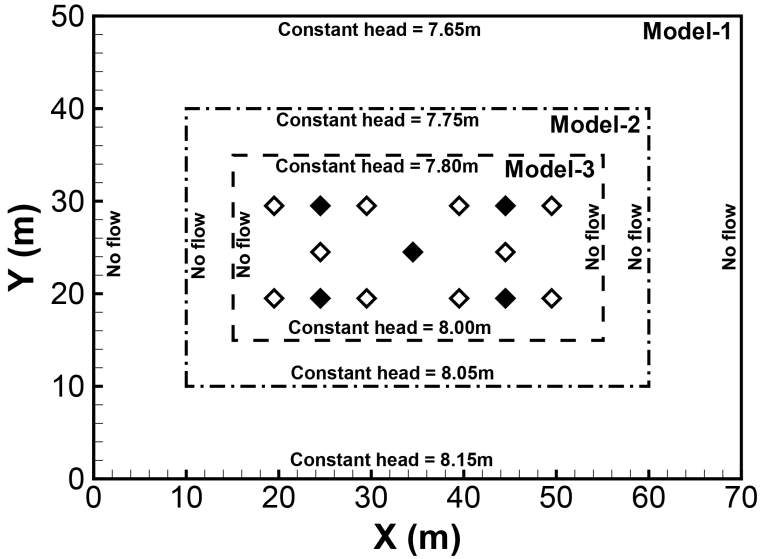

Figure 13. The conceptual models and the sizes of three models. Symbols in the figures show the monitoring and injection well (filled diamonds) locations. The observation data for simulations were kept the same for three models.

HESSD
12, 12567–12613, 2015

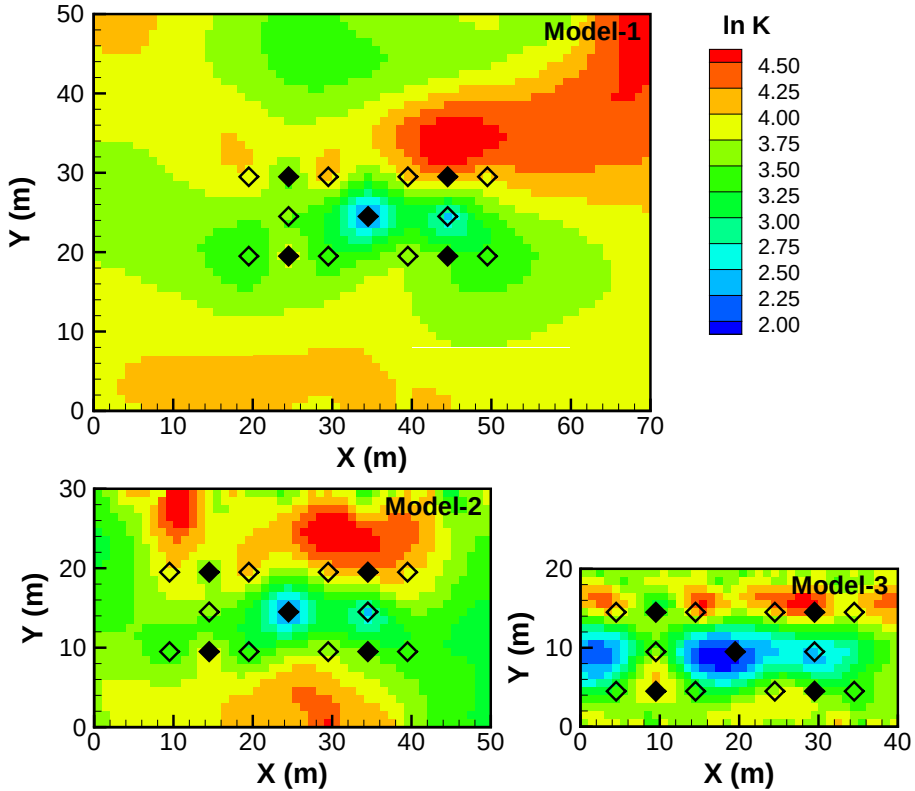

Figure 14. Estimated $\ln K$ fields for the three models.

HESSD
12, 12567–12613, 2015

Sequential hydraulic tests for transient unconfined aquifers

C.-F. Ni et al.

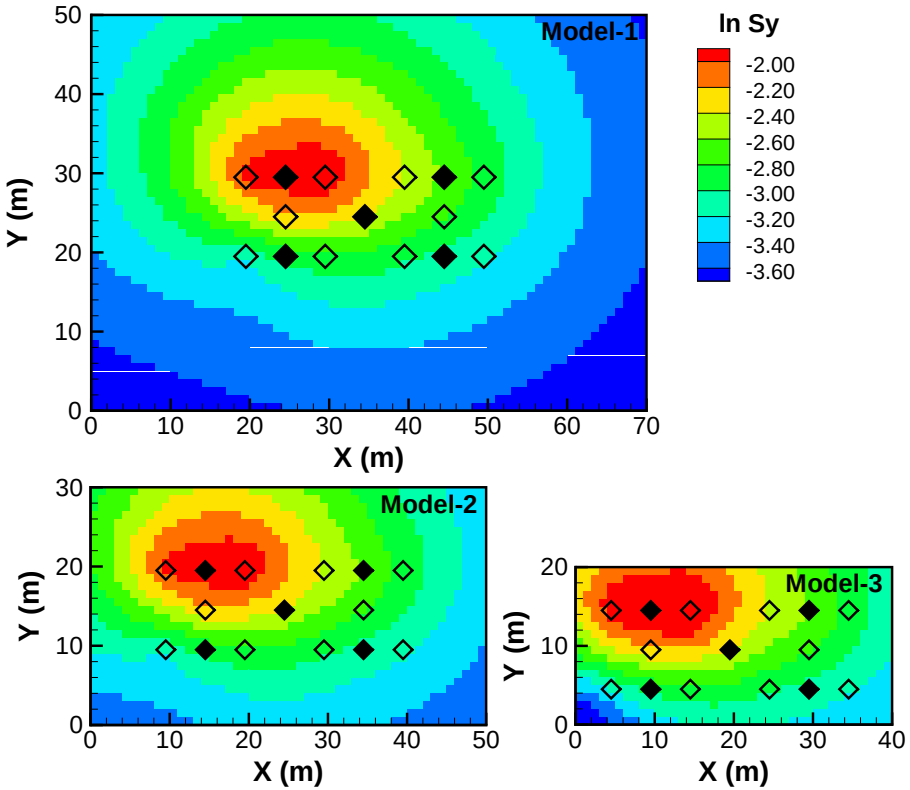

Figure 15. Estimated ln Sy fields for three models.

HESSD
12, 12567–12613, 2015

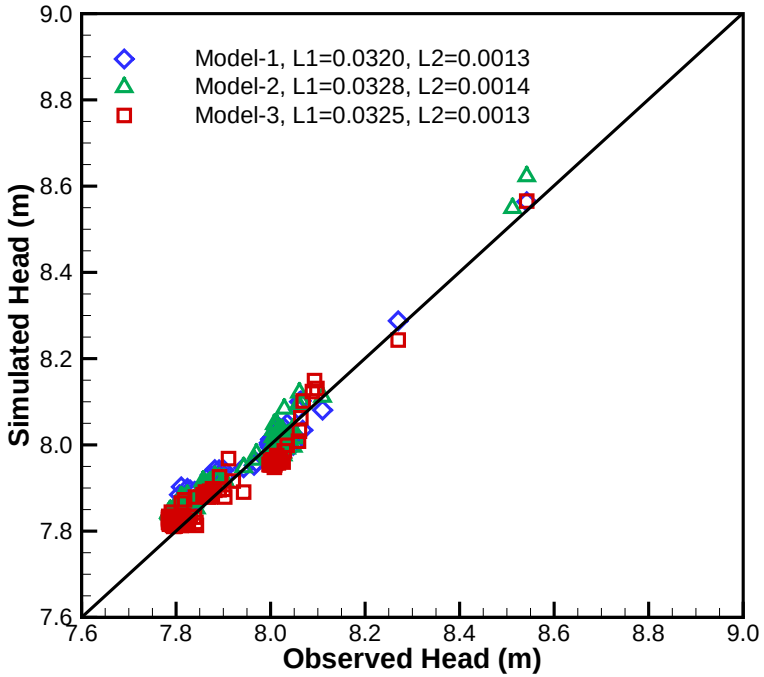

Figure 16. Comparison of simulated and observed head values at selected well locations for the three models.

HESSD
12, 12567–12613, 2015